Solid-state additive manufacturing high performance aluminum alloy 6061 enabled by an in-situ micro-forging assisted cold spray

Ying-Kang Wei [a], Xiao-Tao Luo [a,*], Xin Chu [c], Guo-Sheng Huang [b,**], Chang-Jiu Li [a]

[a] *State Key Laboratory for Mechanical Behavior of Materials, School of Materials Science and Engineering, Xi'an Jiaotong University, Xi'an, Shaanxi, 710049, PR China*
[b] *State Key Laboratory for Marine Corrosion and Protection, Luoyang Ship Material Research Institute (LSMRI), Qingdao, Shandong, 266237, PR China*
[c] *Department of Mining and Materials Engineering, McGill University, Montreal, Quebec, H3A 0C5, Canada*

ARTICLE INFO

ABSTRACT

Cold spraying is a competitive additive manufacturing method featuring several unique characteristics and allows large-scale production of metallic components from a wide range of materials. In literature, high performance cold sprayed aluminum deposits produced using high-cost helium gas have been qualified for various applications. In this study, high performance aluminum alloy 6061 (AA6061) deposits were produced through a cold spray method using low-cost nitrogen gas enabled by an in-situ micro-forging effect (MF-CS). Results show that the MF-CS AA6061 deposit presents very low porosity as well as high ultimate tensile strength (UTS) and elastic modulus (E). Moreover, the MF-CS AA6061 deposit consists of superior equiaxed submicron fine Al grains with random orientations. However, the severe work hardening induced by intensive particle plastic deformation during deposition leads to very low ductility of the MF-CS AA6061 deposit. To eliminate this limitation, three strategies of heat treatments (stress relieving, recrystallization annealing and T6) were performed to the MF-CS AA6061 deposit. It was found that heat treatment generated complex effects on both inter-particle bonding and inner-particle microstructure (grain size, dislocation density and precipitation) and different strategies lead to different mechanical properties of AA6061 deposits. Among them, T6 heat-treated AA6061 deposits give the best overall mechanical properties with comparable UTS and E and only slightly inferior ductility to the corresponding T6 bulk.

1. Introduction

Metal-based additive manufacturing (AM), which directly makes three-dimensional components by depositing layer by layer as opposed to subtractive techniques, is a potentially disruptive technology in various industries such as aerospace, automotive and biomedical. Building up metal components by AM processes can promote design freedom and manufacturing flexibility, therefore enabling intricate structure production, enhanced product customization and shorter time to market while eliminating conventional economy-of-scale restraints [1]. So far, many fusion-based AM methods have been well developed, such as selective laser melting (SLM), laser engineered net shaping (LENS), laser metal deposition (LMD), and electron beam melting (EBM) [1,2]. However, laser-based AM processes are not efficient to build parts from materials with high-reflectivity, e.g. aluminum (Al) and copper (Cu) alloys [3]. EBM AM can usually produce high "quality" components but is less common in commercial markets due to the cost of high vacuum requirements and relatively low efficiency [4]. Cold spray (CS), in which micron-sized particles (5–70 μm) are accelerated to supersonic velocities by compressed gas (nitrogen (N_2), helium (He) or air) in a De-Laval nozzle to deposit on the substrate, is an emerging AM process (ISO/ASTM52900-15 [5]) and is receiving growing interest due to its low processing temperature (<1000 °C and material dependent) [6–8]. Different to fusion-based AM methods, cold sprayed deposits are built up by accumulated particle bonding in the solid state through severe particle plastic deformation upon high velocity impact. Cold spray is reported to be particularly suitable for additive manufacturing high reflectivity metals (e.g. Cu and Al) that are often challenging using laser-based AM processes [9]. Moreover, cold spray also exhibits many unique advantages, such as unlimited component size, no need for protective gas atmosphere, minimized oxidation, equiaxed grains, no residual stress induced cracking, and ease in producing composites [7].

---

* Corresponding author.
** Corresponding author.
  E-mail addresses: luoxiaotao@mail.xjtu.edu.cn (X.-T. Luo), huanggs@sunrui.net (G.-S. Huang).

Aluminum alloy 6061 (AA6061) is an extensively used high performance engineering alloy in aerospace and automobile industries due to its high strength to weight ratio and good corrosion resistance. For industrial applications, mechanical properties (especially tensile strength) of additively manufactured parts are of significant concern; and for CS metallic components they often depend on the levels of defects and inter-particle bonding [10]. Generally, the presence of inter-particle pores and poorly bonded inter-particle boundaries reduces the effective area to resist tensile pull-off; the latter can also generate preferential stress concentration leading to fast crack propagation along inter-particle boundaries. Table 1 summarizes the detailed spray parameters as well as corresponding porosity and mechanical properties (yield strength (YS), ultimate tensile strength (UTS), elongation and elastic modulus (E)) of CS AA6061 and other Al alloy deposits from literature. As shown, porosity commonly exists in conventional CS AA6061 deposits when using N_2 as accelerating gas (CS–N_2) due to insufficient particle plastic deformation during deposition [11,12]. For instance, Aldwell et al. [12] reported that the porosity of CS-N_2 AA6061 deposits is high as ~ 8% at gas temperature and pressure of 400 °C and 2 MPa, respectively. To overcome these limits, two main strategies can be usually employed: i) thermally soften the feedstock to lower its resistance to plastically deform and ii) increase the particle velocity to enhance the "driving force" for plastic deformation. Usually, higher gas temperature and pressure result in higher particle temperatures and velocities, and thereby more compact deposits [13–15]. For example, Murray et al. [14] prepared high density (porosity: 1%) CS-N_2 Al alloy C355 (Al–5Si–1Cu–Mg) with N_2 at high gas temperature and pressure of 500 °C and 6 MPa, respectively. However, for low melting point Al alloys, increasing gas temperature also increases the possibility of blocking the spray nozzle (if the nozzle material is not specially designed) and thus interrupting continuous spraying process. On the other hand, higher gas pressure leads to higher gas consumption and thus cost (e.g. > 1200 l min^{-1} when gas pressure is > 5 MPa). Using He instead of N_2 as processing gas (CS–He) is a more straightforward approach to increase the particle velocity and temperature and thus results in denser deposits due to its lower gas density and higher specific heat [8]. Many researchers [16–18] prepared fully dense CS-He AA6061 deposits with relatively high strength at gas temperature and pressure of above 400 °C and 2 MPa, respectively. For instance, Rokni et al. [16] reported that the ultimate tensile strength (UTS) of CS-He AA6061 is higher than 400 MPa; whereas the value of wrought bulk AA6061-O is only about 120 MPa [19]. These high performance CS-He AA6061 deposits have been qualified for various applications from free-standing components fabrication (e.g. tube and flange [8]) and damaged components repair (e.g. magnesium gearbox [17]) in the last decades. However, using the high-cost and nonrenewable helium gas requires a gas recycling facility to be installed for industrial scale production which demands a large initial investment.

Generally, as-prepared CS deposits exhibit very limited plasticity compared with the corresponding bulk due to the severe work hardening induced by intensive particle plastic deformation during solid-state deposition and the relatively poor inter-particle bonding [20]. Heat treatment (HT) is a commonly used approach to optimize the microstructure and thus improve the mechanical properties of AM metallic

components. Post-spray heat treatment can effectively improve inter-particle bonding (metallurgical bonding) through solid-state diffusion and eliminate dislocation density to improve the ductility of CS deposits [20,21]. Moreover, heat treatment can alter the inner-particle microstructure (e.g. grain size and phase composition [16] which also affects the mechanical properties. Meanwhile, the characteristics of cold sprayed deposits (e.g. porosity, inter-particle bonding state, amount of particle deformation) can vice versa influence the effectiveness of heat treatment. Therefore, the final effects of heat treatment on microstructure and overall mechanical properties of cold sprayed deposits are complicated and often difficult to predict. Detailed heat treatment studies on a specific cold sprayed deposit should be performed.

Recently, an in-situ micro-forging assisted cold spray process (MF-CS) was developed in the Thermal Spray Lab, Xi'an Jiaotong University [21–23]. Compared to the conventional CS method, in-situ MF-CS process sprays a mixture of spray targeting powders and large-sized (150–300 μm) micro-forging (MF) particles. During deposition, incoming large MF particles with high impact energies in-situ forge and further compact the exposed porous layers (in-situ MF effect). Subsequently, the large-sized MF particles are rebounded off due to the relatively low impact velocity and do not contaminate targeting materials. Moreover, the hard MF particles remain spherical and can be recycled by a special electromagnet device. Previous studies have shown that the MF-CS can be a viable method to achieve dense deposits without using He or high gas temperature for various metals, such as Ti [22], Ti6Al4V [22], Ni [23] and IN718 [21]. In this study, fully dense AA6061 deposits were prepared via the MF-CS process using optimized spraying conditions. The microstructure and mechanical properties of the MF-CS AA6061 deposit were investigated and are discussed. To further improve the overall mechanical properties of MF-CS deposits, three types of post-spray heat treatments were performed to free-standing AA6061 deposits, and the effects of heat treatment conditions on the microstructure and mechanical properties were also investigated.

2. Experiments

2.1. Feedstock preparation

Commercial gas-atomized AA6061 (0.4 wt% Si, 0.9 wt% Mg, 0.2 wt% Fe, 0.15 wt% Mn, 0.2 wt% Cu, bal. Al) powder (14 USD/Kg, BGRIMM Co., Ltd., Beijing, China) and 410 martensitic stainless steel (SS) powder (7 USD/Kg, Wei Guang Shot-peening material Co., Ltd. Wuxi, China) were used as spray targeting and in-situ MF powders, respectively. Fig. S1 presents SEM morphologies and particle size distributions of AA6061 and MF powders. Both AA6061 and MF powders have a spherical morphology. The D10, D50 and D90 values for the AA6061 powder are measured to be 13.2, 25.6 and 42.1 μm, respectively; corresponding values for the MF powder are 217.6, 229.1 and 245.6 μm, respectively. The high hardness (~340 $HV_{0.3}$) of MF particles relative to AA6061 (40 $HV_{0.1}$) ensures the impact induced plastic deformation concentrates on soft AA6061 particles. The feedstock was prepared by mixing 30 vol% of AA6061 with 70 vol% of MF to introduce sufficient in-situ MF effect [21,22]. Powder mixtures were sealed in a plastic vessel

Table 1
The detailed spray parameters and corresponding porosity and mechanical properties (YS, UTS, elongation and E) of CS-N_2 and CS-He Al alloy deposits.

Methods	Materials	Gas temp.(°C)	Gas pres. (MPa)	Porosity (%)	YS (MPa)	UTS (MPa)	Elongation (%)	E (GPa)	References
CS-N_2	AA6061	350	3	14.4	–	–	–	–	[11]
		400	2	8.27	–	–	–	–	[12]
	AA2024	500	3.5	0.41	–	–	–	68.6	[13]
	C355	500	6	1.07	–	~200	~0.65	–	[14]
	A357	450	5.7	~0	–	183–217	~0	62–63	[15]
CS-He	AA6061	400	2	~0	~290	~340	~3	–	[17]
		400	2.8		–	~440	~3	–	[16]
		400	2		262	286.8	2	67.5	[18]

and then admixed using a drum mixer for 2 h at a rotation speed of 40 rpm. After admixing, the feedstock was dried for 1 h in oven at 75 °C and then vacuum sealed for subsequent cold spray. The processes of feedstock preparation are schematically shown in Fig. 1a. Commercially pure Al plates were sectioned into 70 mm × 30 mm × 6 mm pieces and are used as substrates. Prior to spray, substrates were cleaned in an ultrasonic acetone bath for 10 min and then sandblasted with 24 grit alumina by compressed air using 0.6 MPa pressure. The roughness of the blasted substrate surface was measured to be Ra ~10 μm.

2.2. Cold spray

AA6061 deposits were produced using an in-house made cold spray system with an optimized De-Laval nozzle. The convergent-divergent spray nozzle has a 2.4 mm diameter throat, a 200 mm long divergent section, and a 6.25 mm diameter exit. Nitrogen (0.8 USD/m^3) was used as the accelerating gas with a pressure and temperature of 2.5 MPa and 300 °C, respectively. Under current parameters, the mass flow of the nitrogen gas is about 600 l min^{-1}. As illustrated in Fig. 1b, a zig-zag scan strategy was used with a step size of 2 mm. The stand-off distance and traverse speed of the spray gun were set to be 20 mm and 60 mm s^{-1}, respectively. The feedstock powder feeding rate was about 100 g min^{-1}. The MF-CS deposits were produced by spraying multiple passes to obtain an approximate thickness of 35 mm. It should be pointed out that the high content of MF particles will reduce the deposition efficiency (DE) of the AA6061 powder due to severer erosion [21]. In this study, the DE of the AA6061 powder is about 40%, which is slightly lower than that from the CS-N$_2$ method (~60%) under the similar spray parameters. Despite that it still takes only ~10 min to prepare an MF-CS AA6061 deposit (inset of Fig. 1b) with dimensions of 70 mm × 30 mm × 35 mm using current parameters. A commercial optical time-of-flight Cold Spray Meter particle diagnostic system DPV 2000 (DPV evolution, TECNAR Automation Ltd., Canada) was used to measure in-flight velocities (without substrate) of AA6061 and MF particles using same parameters as the deposit fabrication. In this work, the average in-flight velocities of AA6061 and MF particles were measured to be 508 and 235 m s^{-1}, respectively. After the MF-CS process, the substrate was carefully removed by electrical discharge machining and free-standing AA6061 specimens with dimensions of 70 mm × 15 mm × 10 mm were sectioned

for post-spray heat treatment. Images of the AA6061 deposit before and after substrate removal are also shown in Fig. 1b.

2.3. Post-spray heat treatment

Fig. 1c summarizes the post-spray heat treatment conditions used in this study. Three common strategies of heat treatment, i.e. stress relieving (SR), recrystallization annealing (RA) and T6 (solid-solution treatment followed by artificial ageing), were performed to MF-CS AA6061 deposits in an argon atmosphere furnace. Stress relieving is a common heat treatment process for cold deformed metallic products to partially remove the internal residual stress and reduce the tendency of deformation cracking. In this work, the as-deposited AA6061 was heated to 175 °C for 8 h, then subsequently cooled in air to room temperature. Recrystallization annealing is often used to improve the ductility and fracture toughness of cold deformed parts. In this study, the as-deposited deposit was heated to 450 °C for 2 h, then cooled slowly with furnace to room temperature at a rate of 5 °C min^{-1}. T6 is one of the most frequently used heat treatment processes for precipitation hardening alloys to improve the strength and hardness. In this work, the as-deposited AA6061 was solution heat treated to 535 °C for 1 h, water quenched to room temperature, further aged to 175 °C for 4 h, and finally cooled in air to room temperature.

2.4. Mechanical tests and characterization

Volumetric size distributions of the AA6061 and MF powders were measured by a laser particle size analyzer (Horiba LA-920, Horiba, Tokyo, Japan). Morphologies of AA6061 and MF powders and cross-sectional microstructures of AA6061 deposits were characterized by a field emission scanning electron microscope (SEM, MIRA3 LMH, TESCAN, Czech) with an electron backscatter diffraction (EBSD, Nordlys-Nano, Oxford Instruments, UK) system. Slight etching was performed on the finely polished cross-sectional microstructures using 50 g l^{-1} NaOH solution for 10 s at 25 °C to reveal inter-particle boundaries. The porosity of AA6061 deposits was measured using 15 cross-sectional backscattered electron (BSE) images at 1000 × magnification using ImageJ software. The spatial and angular resolutions of the EBSD system were 50 nm and 0.5°, respectively. The acceleration voltage used was
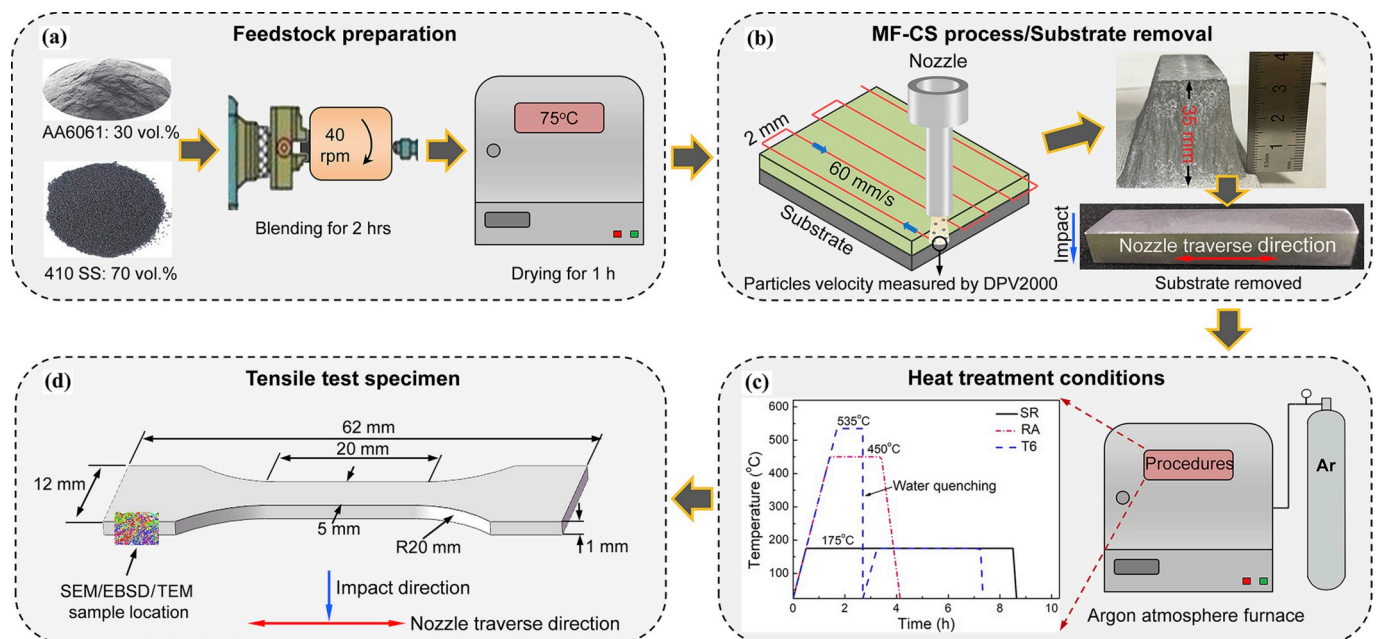

Fig. 1. Schematic diagrams of (a) feedstock preparation, (b) MF-CS process and images of the AA6061 deposit before and after substrate removal, (c) post-spray heat treatment conditions, and (d) dimensions of tensile test specimen.

20 keV and the step size was 100 nm. The recorded EBSD data was post analyzed using Oxford Instruments Channel 5 software. EBSD samples were prepared using standard metallographic methods finished with 0.05 μm colloidal silica suspension followed by electropolishing in 5 ml perchloric acid and 95 ml alcohol for 5 s at - 20 °C. The microstructures of the as-deposited AA6061 were also characterized by a transmission electron microscope (TEM, JEM-F200, JEOL, Japan) at 200 keV. Tensile tests were performed according to the ISO 6892-1 standard [24]. The plate tensile specimens were machined by electrical discharge method along the gun traverse direction to dimensions as shown in Fig. 1d. The specimens were ground by 1200 grit abrasive paper to obtain a relatively smooth finish of Ra ~0.5. Uniaxial tensile tests were performed to both as-deposited and heat-treated AA6061 samples using an MTS material testing machine (MTS Systems Corporation, Minneapolis, MN, USA) at a cross head speed of 0.2 mm min^{-1}. Minimum three samples at each condition were used for each measurement. The extension of the tensile specimen was recorded by a clip-on extensometer during uniaxial tension test. Samples were pulled apart until fracture and fractured surfaces were characterized using SEM.

3. Results

3.1. Microstructure and mechanical properties of MF-CS AA6061

Fig. 2a shows the as-polished cross-sectional SEM-BSE images of MF-CS AA6061 deposits. As shown, the MF-CS AA6061 deposit presents a fully dense microstructure while microstructural defects (inter-particle pores and debonding) are rarely observed even at 5000× magnification (inset of Fig. 2a). Note that, as a comparison, conventional SLM fabricated AA6061 components are usually reported to present periodic columnar cracks due to the high crack sensitivity of Al–Si–Mg systems during rapid solidification which seriously deteriorates their performance [19,25,26]. The porosity of the MF-CS AA6061 deposit was measured to be only 0.12%, which is similar to the value of high quality CS-N$_2$ Al alloys deposits sprayed at extremely high parameters [13–15] or CS-He AA6061 deposits [16–18]. Furthermore, no MF particle was found in the MF-CS deposit and contamination of the stainless steel MF particle to the Al-based deposit was avoided although a high volume (70 vol%) of MF particles was mechanically blended into the initial AA6061 spraying powder. This is attributed to the relatively low impact velocity and spherical morphology of the MF particles. In fact, inclusions of angular-shaped ceramic particles into soft metallic coatings due to penetration have been frequently observed when mechanically mixed ceramic and metallic particles are used to prepare composite coatings [27]. It was found that the penetration depth is linearly positive to the particle velocity and higher penetration depth indicates easier penetration and contamination [28]. Acceleration of the particles in gas flows are highly dependent on particle size, where larger particles lead to lower velocity due to the higher inertia and vice-versa for smaller particles. In this study, the relatively large size (200–300 μm) of the MF particles results in low velocities (235 m s^{-1}) and therefore shallower penetration. On the other hand, different from the angular shape by which high level of stress could be generated at sharp edges of the

ceramic particles as they impact on the soft metallic layer and thus result in severe penetration, the spherical morphology of stainless steel MF particles could greatly decrease the stress concentration and thus avoid penetration. Overall, the above results show that in-situ MF effect can produce fully dense CS AA6061 deposit using the cost-effective N$_2$ processing gas.

Mechanical properties (YS, UTS, elongation) of MF-CS AA6061 deposits were measured via room temperature tensile tests and the results are presented in Fig. 2b. Values of LAM fabricated AA6061 [19] and wrought bulk AA6061-O [19] are also tabulated for reference. Compared with LAM fabricated AA6061 and wrought bulk AA6061-O, an improvement in strength could be clearly observed for the MF-CS AA6061 deposits (~280 MPa for UTS). However, the elongation of the MF-CS AA6061 deposit is only about 0.6%, which is much lower than that of the LAM fabricated AA6061 (11–15%) or wrought bulk AA6061-O (30%). The reasons for such unique characteristics of MF-CS AA6061 will be discussed in Section 4.2. Moreover, elastic modulus of the MF-CS AA6061 and bulk AA6061 is also presented in Fig. 2b. As shown, the elastic modulus of the MF-CS AA6061 deposit is 64.3 ± 1.3 GPa, which is equivalent to ~90% of the bulk AA6061. For fully dense bulk metals, elastic modulus stands for the atomic bond stiffness and is not sensitive to the processing. In cold sprayed metals, atoms are metallically bonded within an individual particle which forms the deposit. This indicates that the inter-particle bonding dominates the elastic modulus when the porosity contents are minor and can be neglected. In other words, elastic modulus can be used to evaluate the inter-particle bonding of cold sprayed dense deposits [29]. The close elastic modulus to bulk AA6061 suggests that most inter-particles boundaries in the MF-CS AA6061 deposit have reached metallurgical bonding.

The fracture surface morphologies after tensile tests were also characterized and are shown in Fig. S2. Similar to CS-He AA6061 deposits [16], fracture surfaces of the MF-CS AA6061 deposit exhibit two main features (i) primary dimple features indicative of *trans*-particle fracture (Fig. S2b) and (ii) clear particle profiles (as marked by arrows in Fig. S2a) indicative of inter-particle fracture. The former also suggests some metallurgical bonding was formed in the MF-CS AA6061 deposit. This observation is consistent with elastic modulus results (Table 1).

3.2. Microstructure of heat-treated MF-CS AA6061

The above results show that the MF-CS AA6061 presents high strength and elastic modulus but limited ductility. Heat treatment was thus performed to the MF-CS AA6061 deposit aiming to further enhance its overall mechanical properties. The effects of different heat treatment conditions (SR, RA and T6) on microstructure were firstly studied in this section.

Fig. 3 presents as-etched cross-sectional SEM-BSE microstructures and corresponding porosity of as-deposited and heat-treated MF-CS AA6061 deposits. In the as-deposited AA6061 a few inter-particle gaps are revealed (as denoted by solid arrows in Fig. 3a). After SR heat treatment (Fig. 3b) inter-particle gaps can still be observed. This suggests the SR heat treatment leads to no significant improvement of the inter-particle bonding due to the slow atom diffusion rate at low heat treatment temperature. In contrast, after RA (Fig. 3c) and T6 (Fig. 3d) heat treatments, the inter-particle gaps almost all disappeared. The improved inter-particle bonding after RA and T6 heat treatments can be attributed to the increased diffusion rate at relatively high heat treatment temperatures. Similar improvements are also reported in the CS pure Al deposit after annealing heat treatment at a temperature higher than 300 °C [20]. Moreover, after RA (Fig. 3c) and T6 (Fig. 3d) heat treatments some small (<5 μm) global pores (as marked by ellipses) are observed, which is expected to form via spheroidization and clustering of inter-particle gaps with a tendency to reduce surface energy of these defects. Moreover, the porosity measurements show that as compared to the as-deposited AA6061 (0.12%), the heat-treated AA6061 deposit has similar porosity (0.14%) while RA and T6 treated deposits show
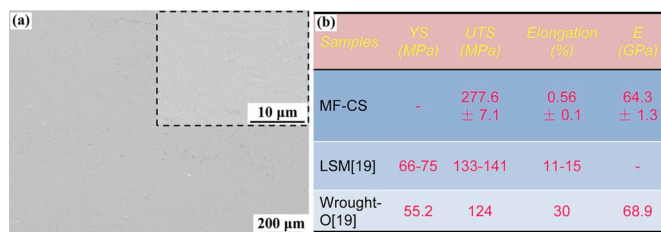

Fig. 2. The cross-sectional microstructure of MF-CS AA6061 deposit (a); Comparison of mechanical properties of MF-CS AA6061 deposits, LAM fabricated AA6061 [19] and wrought bulk AA6061-O [19] (b).
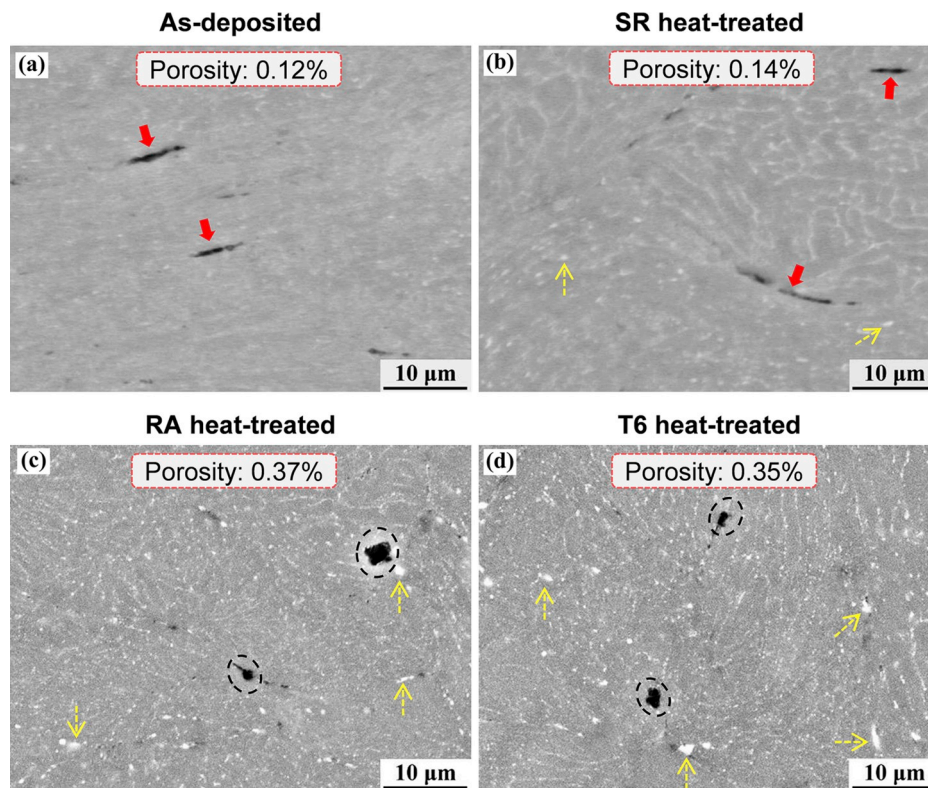
Samples	YS (MPa)	UTS (MPa)	Elongation (%)	E (GPa)
MF-CS	-	277.6 ± 7.1	0.56 ± 0.1	64.3 ± 1.3
LSM[19]	66-75	133-141	11-15	-
Wrought-O[19]	55.2	124	30	68.9

Fig. 3. Slightly etched cross-sections of (a) as-deposited and (b) SR, (c) RA and (d) T6 heat-treated MF-CS AA6061 deposits, respectively.

increments in porosities of 0.37% and 0.35%, respectively.

The cross-sectional microstructures of above AA6061 deposits were also characterized by EBSD with a scan area of 60 μm × 60 μm (larger than one particle). Fig. 4a–d shows EBSD inverse pole figure (IPF) maps of as-deposited and heat-treated AA6061. The grain sizes were calculated and the average values with standard deviations are also presented. In IPF maps, each grain is color coded with respect to the reference crystal orientations provided as an inset in Fig. 4a. It is also noted that white areas in Fig. 4 are unidentified regions and the deposit is fully dense. As shown in Fig. 4a, the as-deposited AA6061 consists of roughly equiaxed submicron grains with random orientations and an average grain size of 0.97 ± 0.56 μm, while in AA6061 feedstock powder the grain size ranges from 4 to 22 μm (not shown here). The grain refinement in CS deposits as compared to the initial feedstock arises from the severe plastic deformation induced dynamic recrystallization during deposition [10]. Moreover, the grain size of the as-deposited AA6061 shows a little variation in different regions: in Fig. 4a, the bottom right corner reveals a slightly finer grain than the upper left corner. For the conventional CS, the limitedly deformed particles usually present a heterogeneous plastic deformation: the closer to the particle interface, the larger degree of plastic deformation. As reported by Rokni et al. [16], the grains at the AA6061 particle interface can be refined to sub-micrometer range while the grains at inner part of the deposited particle are still in ~10 μm. In this work, the plastic deformation of the deposited AA6061 particles was greatly enhanced by the MF particles since the MF particles (200–300 μm) are much larger than the AA6061 particles (10–60 μm). Therefore, the grains in nearly the whole deposited particle could be refined to micrometer size as shown in Fig. 4a. However, as the MF particle induced plastic deformation may still be a little bit non-uniform, the grain size shows a little variation in different regions in the as-deposited MF-CS AA6061 (Fig. 4a). After SR heat treatment, obvious grain growth is not observed and the AA6061 deposit (Fig. 4b) shows a similar average size (1.24 ± 0.54 μm) and size distribution of the grains as compared to the as-deposited AA6061. After RA and T6 heat treatments, grain growth is clearly observed from IPF

maps (Fig. 4c and d) resulting from the static recrystallization during heat treatment (usually > 300 °C for CS AA6061 [30]). The average grain sizes of RA and T6 AA6061 deposits are 11.91 ± 4.9 and 7.76 ± 3.3 μm, respectively. In addition, in all cases evident orientation texture was not observed and grains in all deposits show random orientation distribution.

Fig. 4e–h shows Kernel average misorientation (KAM) maps of as-deposited and heat-treated AA6061 deposits. KAM maps can usually be used to highlight local changes in dislocation density and its distribution [31]. In KAM maps, the average misorientation angle of a point with all of its nearest neighbors was calculated and misorientations exceeding 5° were excluded from calculations. In the as-deposited AA6061, the high degree of plastic deformation causes high dislocations density (work hardening) (shown in green to red shades in Fig. 4e). As compared to the as-deposited AA6061, it is evident that limited recovery has occurred after SR (Fig. 4f) heat treatment. In contrast, by a significant reduction in dislocation density, indicating that significant recovery has occurred in the microstructure of AA6061 deposits during RA (Fig. 4g) and T6 (Fig. 4h) heat treatment.

It is known that β-Mg_2Si is the main precipitation strengthening phase in AA6061. Fig. S4 shows the phase distribution maps of the Al-matrix (red) and Mg_2Si (blue) along with grain boundaries in as-deposited and heat-treated AA6061 deposits. In Fig. 4i no visible Mg_2Si particle can be identified in the as-deposited AA6061, suggesting the MF-CS AA6061 deposit has a single Al phase (fcc structure) without obvious Mg_2Si (fcc structure) precipitations. Bright field TEM (BF-TEM) images at different magnifications (Fig. 5a and b) and corresponding selected area electron diffraction (SAED) patterns (Fig. 5c) were also taken to further confirm this feature. From the BF-TEM images, nano-sized dsc-shaped precipitates particles cannot be observed. One the other hand, all the diffraction spots and rings are indexed to those for fcc Al as is shown in Fig. 5c. The absence of the precipitation in MF-CS AA6061 deposits is attributed to the low processing temperature and short heating period during deposition. Usually, the ultra-high cooling rate (up to 10^5 K s^{-1}) leads to very low level of second-phase particles in
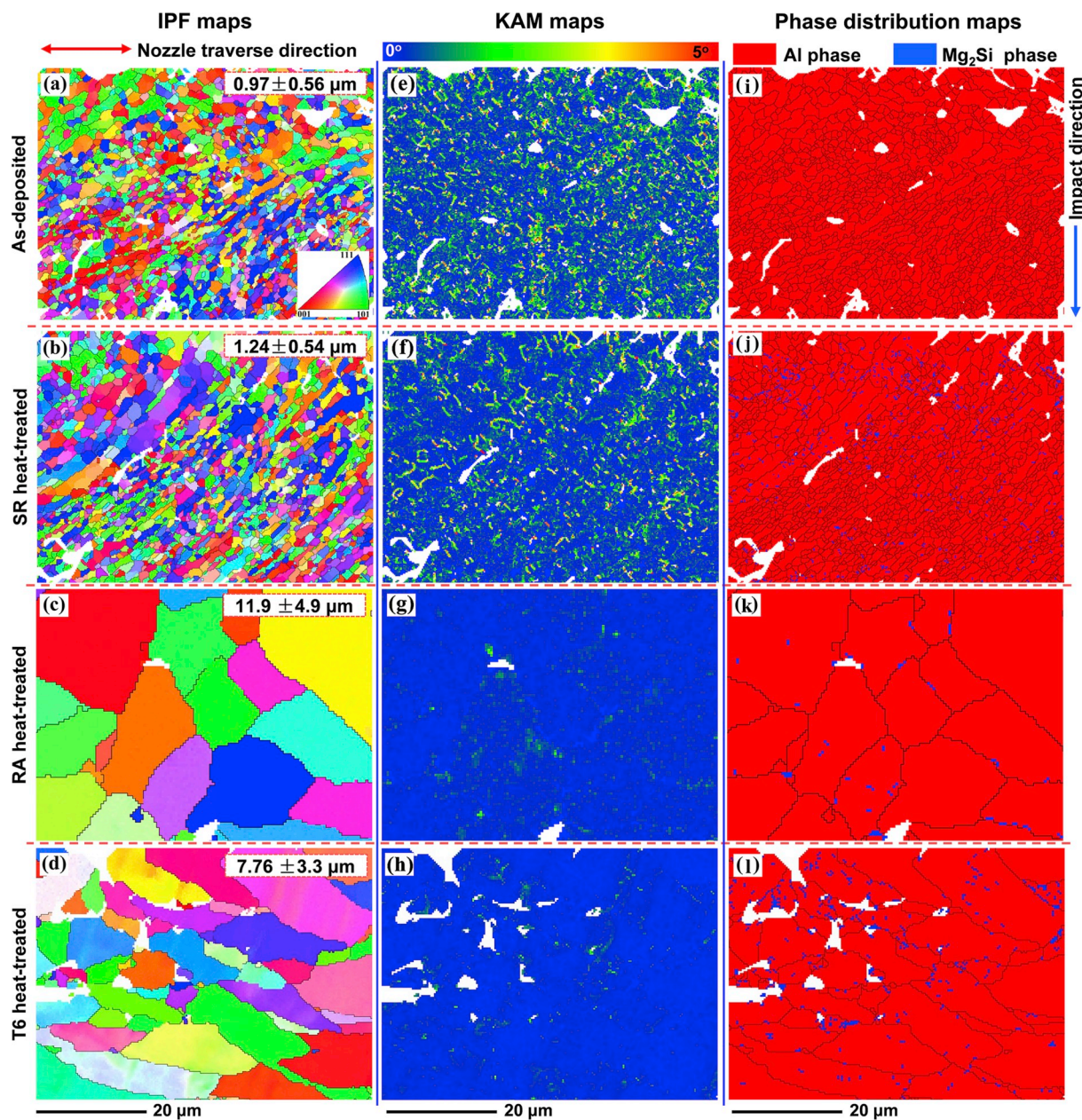
Fig. 4. IPF, KAM and phase distribution maps of (a, e and i) as-deposited and (b, f and j) SR, (c, g and k) RA, and (d, h and l) T6 heat-treated AA6061 deposits, respectively. The white spots are the unidentified regions.
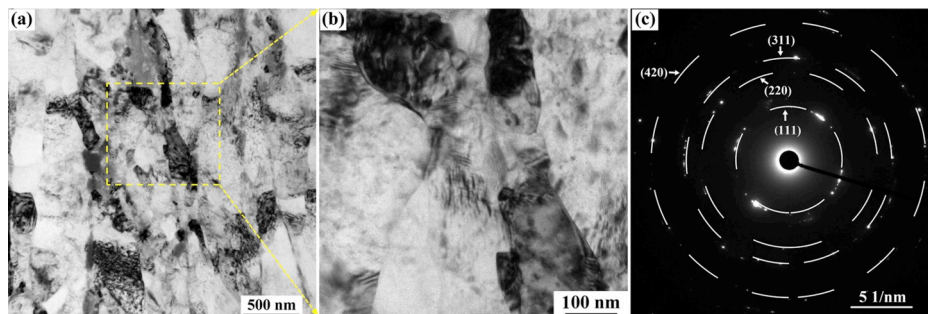

Fig. 5. The BF-TEM image of the as-deposited AA6061 (a); (b) is the closer view of selected region in (a). (c) is SAED patterns corresponding to the whole region in (a).

gas atomized Al alloy powder [32]. During deposition, combination of low accelerating gas temperature (<300 °C) and supersonic particle velocity (~500 m s^{-1}) leads to a very short stay (<0.4 ms) of the AA6061 particles in preheated gas flow (200 mm in length) so that low level of second-phase particles should still remained in the deposit. Rokni et al. [30] similar phenomenon in CS AA6061 deposit by using gas atomized AA6061 powder when the temperature of accelerating He gas is even at 400 °C. Compared with the as-deposited AA6061, after all heat treatment conditions larger-sized (>0.1 μm) Mg$_2$Si particles is clearly observed in phase distribution maps (Fig. 4j-l). The formation of larger-sized precipitates might be attributed to the variation in precipitation behavior caused by the presence of heavily deformed microstructure [16] and further investigation will be performed in the future. As expected, due to the artificial aging, 1.34% and 2.91% area fractions of the Mg$_2$Si phase in SR (Fig. 4j) and T6 (Fig. 4l) heat-treated AA6061 deposits were observed, respectively. Moreover, formation of Mg$_2$Si phase (area fraction of 0.35%) in RA AA6061 deposit (Fig. 4k) might be attributed to the slow cooling rate in the RA heat treatment. Note that, the measured area fraction of Mg$_2$Si particle in this study should be lower than the actual value. In addition to Mg$_2$Si phase, a few impurity phases (iron-rich or copper-rich confirmed by EDS) (<0.5%) are also identified in all heat-treated AA6061 deposits (as marked by dashed arrows in SEM-BSE images in Fig. 3b–d).

3.3. Mechanical properties of heat-treated MF-CS AA6061

Fig. 6 presents the room temperature tensile properties (elastic modulus, YS, UTS and elongation to failure) of heat-treated MF-CS AA6061 deposits. Values of as-deposited AA6061 are also plotted in Fig. 6b for a direct comparison. After SR heat treatment, the AA6061 deposit exhibits slightly higher strength (298.1 ± 9.0 MPa for UTS) but still a limited elongation (~0.9%) before fracture. In contrast, the ductility of AA6061 deposits after RA and T6 heat treatment is significantly improved and the tensile specimen fractures after yielding at strains of ~9.5% (RA) and ~7.5% (T6), respectively. Moreover, it is interesting to note that the RA and T6 heat treatments have opposite effects on the strength of AA6061 deposits. Compared with as-deposited AA6061 (277.6 ± 7.1 MPa), the UTS of RA heat-treated AA6061 deposit decreases to 210.8 ± 5.9 MPa while that of T6 heat-treated AA6061 deposit increases to 314.3 ± 7.9 MPa. The mechanical properties of heat-treated AA6061 deposits will be further discussed in Section 4.2. Also shown in Fig. 6a the AA6061 deposit has similar elastic modulus (63.2 ± 0.7 GPa) after SR heat treatment compared with the as-deposited AA6061 (64.3 ± 1.3 GPa); while after RA and T6 heat treatment the elastic modulus both increase to near bulk AA6061. Furthermore, among all three heat treatment conditions, T6 heat treatment

gives the best overall mechanical properties of MF-CS AA6061 deposits. To better visualize the improvements of in-situ MF effect coupled with T6 heat treatment, the values of UTS and elongation to failure of T6 heat-treated LAM fabricated AA6061 [19] and bulk AA6061 (T6 bulk [16,19] are also plotted in Fig. 6b as a comparison. As shown, the UTS of T6 heat-treated MF-CS AA6061 deposit is close to the T6 heat-treated LAM AA6061 and T6 bulk while the ductility is in between the T6 LAM AA6061 and T6 bulk. Therefore, results show that the MF-CS coupled with post-spray T6 heat treatment can produce high strength AA6061 deposits with satisfactory ductility using nitrogen as the propellant gas.

The fracture manner of the deposits after different heat treatments was examined by fracture morphology as shown in Fig. S3. In Fig. S3a, the SR heat-treated AA6061 deposit presents similar fracture surface morphology to the as-deposited AA6061 (Fig. S2a), revealing *trans*-particle fractures with dimple features (Fig. S3b) and clear particle profiles indicative of inter-particle fractures (as marked by arrows). These observations suggest that both mechanical interlocking and metallurgical bonding exist in SR heat-treated AA6061 deposit. Moreover, in Figs. S3c–f both RA and T6 heat-treated AA6061 deposits show ductile fracture with equiaxed dimples covering the entire fracture surface (except for small pore regions marked by ellipses) and inter-particle fracture is absent, suggesting that full metallurgical inter-particle bonding was formed. Furthermore, it is noted that the size of dimples in as-deposited and SR heat-treated AA6061 deposits is less than 1 μm while the size in RA and T6 heat-treated AA6061 deposits is about 4–10 μm. This observation is consistent with EBSD results (Fig. 4) showing as-reported that the size of dimples is proportional to the grain size [33].

4. Discussion

From Fig. 4a, it can be seen that the as-deposited AA6061 mainly consists of equiaxed submicron grains with random orientations. To further elaborate the advantage of MF-CS process, its grain characteristics (i.e. morphology, size and orientation) are also compared with other aluminum alloy parts fabricated via fusion-based AM methods (i.e. SLM, EBM and wire + arc additive manufacturing (WAAM)) and briefly discussed first in this section.

As compared to wrought bulk AA6061-O, the MF-CS AA6061 deposit presents much higher strength but lower ductility due to its unique microstructures. Moreover, SR, RA and T6 heat treatments present different effects on mechanical properties of the MF-CS deposits and the trend is evidently different from that for the bulk counterpart. To further understand the underlying mechanisms which dominate such an unusual trend, in the second part of this section, the mechanical properties
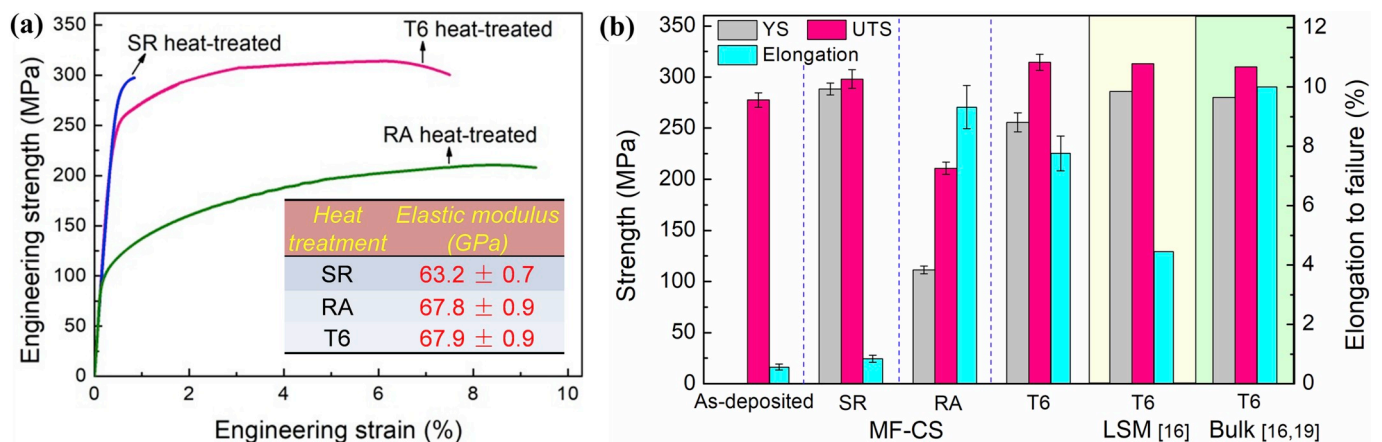

Fig. 6. Characteristic engineering stress-strain curves and elastic modulus of heat-treated AA6061 deposits (a); Comparison of YS, UTS and elongation between as-deposited and different heat-treated samples as well as T6 heat-treated LAM fabricated AA6061 [19] and bulk AA6061 [16,19] (b).

of AA6061 deposits in different conditions (as-deposited and SR, RA, T6 heat-treated) were correlated with their unique microstructural characteristics and are discussed in detail.

4.1. Grain characteristics of as-deposited and heat-treated MF-CS AA6061

Table 2 summarized the detailed morphology, size and orientation of Al-matrix grains in as-deposited and T6 heat-treated MF-CS AA6061 in this study and other aluminum alloy parts fabricated via fusion-based AM methods (SLM [19,34,35], EBM [36] and WAAM [37,38]). The as-deposited MF-CS AA6061 deposit mainly consists of equiaxed submicron-sized grains with random orientations. Even after T6 heat treatment, the equiaxed grains are still finer than 20 μm without preferable orientation. Whereas, for fusion-based AM methods the fabricated aluminum alloys are mainly composed of coarse columnar grains in the melting pool with minor equiaxed grains around melting pool boundaries no matter what type of power sources and raw materials were used. Besides, for SLM Al–5Si–1Cu–Mg reported by Li et al. [34] and EBM AlCoCrFeNi reported by Kuwabara et al. [36], a preferential orientation of columnar grains along the building direction results in the texture development. It is well known that fine-grain metallic materials could favor strength due to Hall-Petch theory. Moreover, fine grains may also improve the corrosion resistance of the aluminum alloys [39]. Last but not least, as compared with equiaxed grains, columnar grains can cause more significant anisotropy issue in mechanical properties [40]. Considering the above aspects, MF-CS method could potentially produce competitive high performance AM metallic components due to obvious advantages in grain characteristics.

4.2. Mechanical properties of as-deposited and heat-treated MF-CS AA6061

In general, the strength and ductility of fully dense CS deposit is determined by combined effects of (i) inter-particle bonding and (ii) inner-particle microstructure [10]. Poorly bonded inter-particle boundaries can usually generate preferential stress concentration leading to fast crack propagation along inter-particle boundaries, thus deteriorating both strength and ductility. In this study, the fracture surface morphologies presented in Fig. S2 indicate that in-situ MF effect is beneficial for inter-particle metallurgical bonding formation. Moreover, the relatively high elastic modulus of the MF-CS AA6061 deposit further indicates that most inter-particle boundaries have formed metallurgical bonding. Therefore, it is not likely that inter-particle bonding state would weaken the strength and ductility of MF-CS AA6061 deposit. The typical characteristics inside deposited AA6061

particles after MF-CS are metastable microstructures induced by severe particle plastic deformation such as refined grains (Fig. 4a) and high density of dislocations (Fig. 4e). Grain refinement is one of the most common strengthening methods for metals. Moreover, high density of dislocations in metallic materials has positive effect on strength but negative effect on ductility. Therefore, in this study, both significant grain refinement and work hardening effects are responsible for the higher strength of the MF-CS AA6061 deposit than wrought bulk counterparts; whereas the work hardening effect itself should be accountable for its poor ductility.

As shown in Section 3.2, post-spray heat treatments (SR, RA and T6) could influence the microstructure of deposited AA6061 particles through many aspects, e.g. inter-particle bonding, grain growth, static recovery, and precipitations of strengthening Mg_2Si phase. The strengthening mechanisms in as-deposited and heat-treated AA6061 deposits are qualitatively discussed and compared in a radar chart in Fig. 7 based on the EBSD and TEM results. There are generally four types of strengthening mechanisms for alloys: solid solution, grain refinement, dislocation multiplication induced work hardening and precipitation strengthening. Since the as-deposited AA6061 is a solid solution phase without precipitation and has high dislocation density and fine grains of 0.97 ± 0.56 μm, solid solution, work hardening and grain refinement are the dominant strengthening mechanisms. In particular, the significant work hardening leads to its poor ductility. In SR heat treatment, due to the relatively low temperature there is no evident change in grain size but some precipitates were formed (Fig. 4j) due to aging and dislocation density decreased due to recovery. These microstructural evolutions suggest that grain refinement and work hardening would still remain; whereas the initial solid solution strengthening would transform to stronger precipitation strengthening and thus lead to the slightly higher strength. Since work hardening is not weakened and inter-particle bonding quality cannot be greatly improved at such a low temperature, ductility is still very poor (0.9%). During RA heat treatment, the high temperature results in full recovery as well as evident recrystallization and grain growth, and the final cooling step (5 °C min^{-1} for rate) does not allow optimized precipitation. The AA6061 deposit features the low dislocation density, relatively coarse grains (11.91 ± 4.9 μm) and few large-sized precipitates (Fig. 4k). Consequently, although solid solution strengthening still remains (slightly weakened), reduced contributions of work hardening and grain refinement lead to a much lower
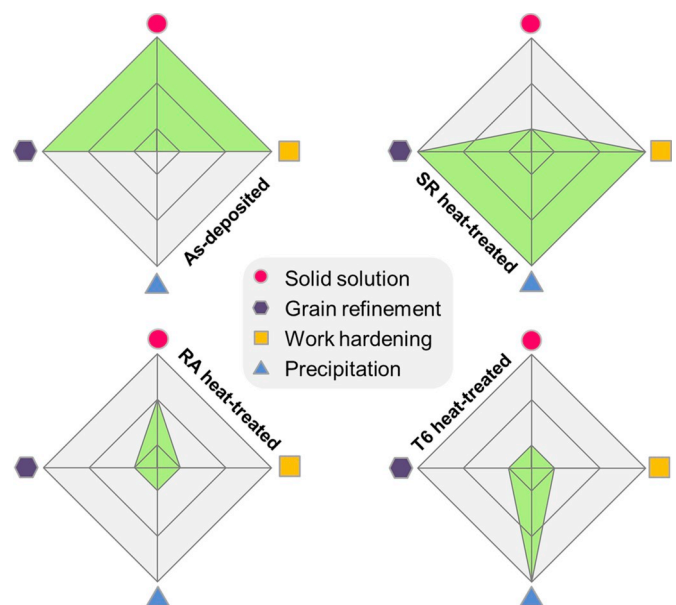
Table 2

A summary of morphology, size and orientation of Al-matrix grains in as-deposited and T6 heat-treated MF-CS AA6061 in this study and aluminum alloy parts fabricated by SLM [19,34,35], EBM [36] and WAAM [37,38].

AM methods	Fabricated Materials	Grain morphology and size (μm)	Orientation
MF-CS	AA6061	Roughly equiaxed: 0.5–4/2–20 for as-deposited/T6	Random
SLM	AA6061 [19]	Columnar: ~40 for widths, ~400 for lengths	–
	Al–5Si–1Cu-Mg [34]	Columnar: 100 for widths; equiaxed: 50-200	<001>
	AlSi10Mg [35]	Columnar: ~20 for widths: ~50 for lengths	–
EBM	AlCoCrFeNi [36]	Columnar: ~5 for widths, ~60 for lengths	<100>
WAAM	AA5356 [37]	Coarse columnar; equiaxed: ~5-50	–
	Al-Cu-Mg [38]	Coarse columnar; equiaxed: ~10-30	–

Fig. 7. Radar chart of strengthening mechanisms in as-deposited and SR, RA and T6 heat-treated AA6061 deposits.

strength. However, the greatly weakened work hardening and much improved inter-particle bonding result in significant improvements in ductility and a relatively high elongation of ~10% is achieved. Moreover, it is worth noting that the very few poorly bonded interfaces were healed due to the highly activated atom diffusion (sintering) during high temperature RA treatment, leading to the increased elastic modulus. After T6 heat treatment, although solid solution, grain refinement and work hardening effects were much weakened, precipitation strengthening becomes remarkable (Fig. 4l), which leads to significant increase in strength. Similar to RA heat treatment, the increase of ductility (~8% for elongation) and elastic modulus after T6 heat treatment can also be attributed to the weakening of work hardening and healing of poorly bonded interfaces.

5. Conclusion

In this study, fully dense (porosity: 0.12%) AA6061 deposits were successfully fabricated via a cost-effective in-situ micro-forging assisted cold spray (MF-CS) method at relatively mild conditions (not very high gas temperature and pressure, no helium). The MF-CS AA6061 deposits present satisfactory ultimate tensile strength (UTS) (277.6 ± 7.1 MPa) and acceptable elastic modulus (64.3 ± 1.3 GPa). However, dense dislocations induced by severe particle plastic deformation still result in the low ductility (<1%) of the MF-CS AA6061 deposit. To further improve mechanical properties, three types of heat treatments, i.e. stress relieving (SR), recrystallization annealing (RA) and T6, were performed to the MF-CS deposited AA6061. The SR heat-treated AA6061 MF-CS deposit presents similar mechanical properties as compared with the as-deposited MF-CS AA6061 due to its limited modification on microstructure at relatively low temperature. After RA heat treatment, AA6061 deposit shows a remarkable decrease in strength (210.8 ± 5.9 MPa) due to static recovery and grain growth. In contrast, the increase in strength after T6 heat treatment (314.3 ± 7.9 MPa, similar to T6 bulk) is mainly caused by precipitation of strengthening phase (Mg_2Si). Moreover, the improved ductility of RA (9.32 ± 0.73%) and T6 (7.76 ± 0.58%) heat-treated deposits can be mainly explained by nearly elimination of work hardening. Furthermore, full formation of inter-particle metallurgical bonding due to sintering effect enhances the elastic modulus of RA and T6 heat-treated AA6061 deposits to near bulk AA6061.

To sum, among all three heat treatment conditions, T6 heat treatment gives the best overall mechanical properties of AA6061 deposits. In addition, although T6 heat-treated AA6061 deposits present an inferior ductility as compared with the bulk counterpart (about 20% lower), the obtained results encourage further investigation for improving the ductility by using powders with low oxygen content and optimizing the heat treatment conditions.

Data availability

The raw/processed data required to reproduce these findings cannot be shared at this time as the data also forms part of an ongoing study.

Author contribution statement

W.-Y. Wei prepared the MF-CS AA6061 deposits, characterized the microstructure and mechanical properties of the deposits, and wrote the manuscript.

X. Chu helped to prepare the heat-treated samples.

X.-T Luo, G.-S. Huang and C.-J. Li designed the experimental programme, coordinated the overall project and provided research funding.

Acknowledgments

Appendix A. Supplementary data

Supplementary data to this article can be found online at https://doi.org/10.1016/j.msea.2020.139024.

References

[1] D. Herzog, V. Seyda, E. Wycisk, C. Emmelmann, Additive manufacturing of metals, Acta Mater. 117 (2016) 371–392, https://doi.org/10.1016/j.actamat.2016.07.019.

[2] J.H. Tan, W.L.E. Wong, K.W. Dalgarno, An overview of powder granulometry on feedstock and part performance in the selective laser melting process, Addit. Manuf. 18 (2017) 228–255, https://doi.org/10.1016/j.addma.2017.10.011.

[3] C. Brice, R. Shenoy, M. Kral, K. Buchannan, Precipitation behavior of aluminum alloy 2139 fabricated using additive manufacturing, Mater. Sci. Eng., A 648 (2015) 9–14, https://doi.org/10.1016/j.msea.2015.08.088.

[4] D. Cormier, O. Harrysson, T. Mahale, H. West, Freeform fabrication of titanium aluminide via electron beam melting using prealloyed and blended powders, Ann. Mater. Sci. Eng. 2007 (2007), https://doi.org/10.1155/2007/34737.

[5] ISO/ASTM52900-15, Standard Terminology for Additive Manufacturing—General Principles—Terminology, ASTM International, West Conshohocken, PA, 2015, https://doi.org/10.1520/ISOASTM52900-15.

[6] W. Li, K. Yang, S. Yin, X. Yang, Y. Xu, R. Lupoi, Solid-state additive manufacturing and repairing by cold spraying: a review, J. Mater. Sci. Technol. 34 (3) (2018) 440–457, https://doi.org/10.1016/j.jmst.2017.09.015.

[7] R. Raoelison, C. Verdy, H. Liao, Cold gas dynamic spray additive manufacturing today: deposit possibilities, technological solutions and viable applications, Mater. Des. 133 (2017) 266–287, https://doi.org/10.1016/j.matdes.2017.07.067.

[8] S. Yin, P. Cavaliere, B. Aldwell, R. Jenkins, H. Liao, W. Li, R. Lupoi, Cold spray additive manufacturing and repair: fundamentals and applications, Addit. Manuf. 21 (2018) 628–650, https://doi.org/10.1016/j.addma.2018.04.017.

[9] S. Yin, R. Jenkins, X. Yan, R. Lupoi, Microstructure and mechanical anisotropy of additively manufactured cold spray copper deposits, Mater. Sci. Eng., A 734 (2018) 67–76, https://doi.org/10.1016/j.msea.2018.07.096.

[10] H. Assadi, H. Kreye, F. Gärtner, T. Klassen, Cold spraying–A materials perspective, Acta Mater. 116 (2016) 382–407, https://doi.org/10.1016/j.actamat.2016.06.034.

[11] Y.-K. Wei, X.-T. Luo, C.-X. Li, C.-J. Li, Optimization of in-situ shot-peening-assisted cold spraying parameters for full corrosion protection of Mg alloy by fully dense Al-based alloy coating, J. Therm. Spray Technol. 26 (1–2) (2017) 173–183, https://doi.org/10.1007/s11666-016-0492-7.

[12] B. Aldwell, E. Kelly, R. Wall, A. Amaldi, G.E. O'Donnell, R. Lupoi, Machinability of Al 6061 deposited with cold spray additive manufacturing, J. Therm. Spray Technol. 26 (7) (2017) 1573–1584, https://doi.org/10.1007/s11666-017-0586-x.

[13] P. Sirvent, M.A. Garrido, C.J. Múnez, P. Poza, S. Vezzù, Effect of higher deposition temperatures on the microstructure and mechanical properties of Al 2024 cold sprayed coatings, Surf. Coating. Technol. 337 (2018) 461–470, https://doi.org/10.1016/j.surfcoat.2018.01.055.

[14] J. Murray, M. Zuccoli, T. Hussain, Heat treatment of cold-sprayed C355 Al for repair: microstructure and mechanical properties, J. Therm. Spray Technol. 27 (1–2) (2018) 159–168, https://doi.org/10.1007/s11666-017-0665-z.

[15] K. Petráčková, J. Kondas, M. Guagliano, Mechanical performance of cold-sprayed A357 aluminum alloy coatings for repair and additive manufacturing, J. Therm. Spray Technol. 26 (8) (2017) 1888–1897, https://doi.org/10.1007/s11666-017-0643-5.

[16] M. Rokni, C. Widener, O. Ozdemir, G. Crawford, Microstructure and mechanical properties of cold sprayed 6061 Al in As-sprayed and heat treated condition, Surf. Coating. Technol. 309 (2017) 641–650, https://doi.org/10.1016/j.surfcoat.2016.12.035.

[17] ARL Center for Cold Spray, Cold Spray for Repair of Magnesium Gearboxes, 2011. https://apps.dtic.mil/dtic/tr/fulltext/u2/a599916.pdf. (Accessed 15 August 2019).

[18] A.G. Gavras, D.A. Lados, V.K. Champagne, R.J. Warren, Effects of processing on microstructure evolution and fatigue crack growth mechanisms in cold-spray 6061 aluminum alloy, Int. J. Fatig. 110 (2018) 49–62, https://doi.org/10.1016/j.ijfatigue.2018.01.006.

[19] S.Z. Uddin, L.E. Murr, C.A. Terrazas, P. Morton, D.A. Roberson, R.B. Wicker, Processing and characterization of crack-free aluminum 6061 using high-temperature heating in laser powder bed fusion additive manufacturing, Addit. Manuf. 22 (2018) 405–415, https://doi.org/10.1016/j.addma.2018.05.047.

[20] R. Huang, M. Sone, W. Ma, H. Fukanuma, The effects of heat treatment on the mechanical properties of cold-sprayed coatings, Surf. Coating. Technol. 261 (2015) 278–288, https://doi.org/10.1016/j.surfcoat.2014.11.017.

[21] X.-T. Luo, M.-L. Yao, N. Ma, M. Takahashi, C.-J. Li, Deposition behavior, microstructure and mechanical properties of an in-situ micro-forging assisted cold spray enabled additively manufactured Inconel 718 alloy, Mater. Des. 155 (2018) 384–395, https://doi.org/10.1016/j.matdes.2018.06.024.

[22] X.-T. Luo, Y.-K. Wei, Y. Wang, C.-J. Li, Microstructure and mechanical property of Ti and Ti6Al4V prepared by an in-situ shot peening assisted cold spraying, Mater. Des. 85 (2015) 527–533, https://doi.org/10.1016/j.matdes.2015.07.015.

[23] Y.-K. Wei, Y.-J. Li, Y. Zhang, X.-T. Luo, C.-J. Li, Corrosion resistant nickel coating with strong adhesion on AZ31B magnesium alloy prepared by an in-situ shot-peening-assisted cold spray, Corrosion Sci. 138 (2018) 105–115, https://doi.org/10.1016/j.corsci.2018.04.018.

[24] ISO 6892-1, Metallic Materials-Tensile Testing- Part 1: Method of Test at Room Temperature, International Organization for Standardization (ISO), Geneva, Switzerland, 2016.

[25] C.E. Roberts, D. Bourell, T. Watt, J. Cohen, A novel processing approach for additive manufacturing of commercial aluminum alloys, Phys. Procedia 83 (2016) 909–917, https://doi.org/10.1016/j.phpro.2016.08.095.

[26] J.H. Martin, B.D. Yahata, J.M. Hundley, J.A. Mayer, T.A. Schaedler, T.M. Pollock, 3D printing of high-strength aluminium alloys, Nature 549 (7672) (2017) 365, https://doi.org/10.1038/nature23894.

[27] Y. Wang, B. Normand, N. Mary, M. Yu, H. Liao, Microstructure and corrosion behavior of cold sprayed SiCp/Al 5056 composite coatings, Surf. Coating. Technol. 251 (2014) 264–275, https://doi.org/10.1016/j.surfcoat.2014.04.036.

[28] L. Murr, S.A. Quinones, A. Ayala, O.L. Valerio, F. Hörz, R. Bernhard, The low-velocity-to-hypervelocity penetration transition for impact craters in metal targets, Mater. Sci. Eng., A 256 (1–2) (1998) 166–182, https://doi.org/10.1016/S0921-5093(98)00796-5.

[29] J. Matejicek, S. Sampath, D. Gilmore, R. Neiser, In situ measurement of residual stresses and elastic moduli in thermal sprayed coatings: Part 2: processing effects on properties of Mo coatings, Acta Mater. 51 (3) (2003) 873–885, https://doi.org/10.1016/S1359-6454(02)00477-9.

[30] M. Rokni, C. Widener, V. Champagne, Microstructural stability of ultrafine grained cold sprayed 6061 aluminum alloy, Appl. Surf. Sci. 290 (2014) 482–489, https://doi.org/10.1016/j.apsusc.2013.11.127.

[31] P.O. Guglielmi, M. Ziehmer, E.T. Lilleodden, On a novel strain indicator based on uncorrelated misorientation angles for correlating dislocation density to local strength, Acta Mater. 150 (2018) 195–205, https://doi.org/10.1016/j.actamat.2018.03.009.

[32] C. Si, X. Tang, X. Zhang, J. Wang, W. Wu, Characteristics of 7055Al alloy powders manufactured by gas-solid two-phase atomization: a comparison with gas atomization process, Mater. Des. 118 (2017) 66–74, https://doi.org/10.1016/j.matdes.2017.01.028.

[33] G. Huang, Y. Shen, The effects of processing environments on the microstructure and mechanical properties of the Ti/5083Al composites produced by friction stir processing, J. Manuf. Process. 30 (2017) 361–373, https://doi.org/10.1016/j.jmapro.2017.10.007.

[34] J. Li, X. Cheng, Z. Li, X. Zong, S.-Q. Zhang, H.-M. Wang, Improving the mechanical properties of Al-5Si-1Cu-Mg aluminum alloy produced by laser additive manufacturing with post-process heat treatments, Mater. Sci. Eng., A 735 (2018) 408–417, https://doi.org/10.1016/j.msea.2018.08.074.

[35] L. Thijs, K. Kempen, J.-P. Kruth, J. Van Humbeeck, Fine-structured aluminium products with controllable texture by selective laser melting of pre-alloyed AlSi10Mg powder, Acta Mater. 61 (5) (2013) 1809–1819, https://doi.org/10.1016/j.actamat.2012.11.052.

[36] K. Kuwabara, H. Shiratori, T. Fujieda, K. Yamanaka, Y. Koizumi, A. Chiba, Mechanical and corrosion properties of AlCoCrFeNi high-entropy alloy fabricated with selective electron beam melting, Addit. Manuf. 23 (2018) 264–271, https://doi.org/10.1016/j.addma.2018.06.006.

[37] L. Wang, Y. Suo, Z. Liang, D. Wang, Q. Wang, Effect of titanium powder on microstructure and mechanical properties of wire+ arc additively manufactured Al-Mg alloy, Mater. Lett. 241 (2019) 231–234, https://doi.org/10.1016/j.matlet.2019.01.117.

[38] Z. Qi, B. Cong, B. Qi, H. Sun, G. Zhao, J. Ding, Microstructure and mechanical properties of double-wire+ arc additively manufactured Al-Cu-Mg alloys, J. Mater. Sci. Technol. 255 (2018) 347–353, https://doi.org/10.1016/j.jmatprotec.2017.12.019.

[39] R. Gupta, D. Fabijanic, R. Zhang, N. Birbilis, Corrosion behaviour and hardness of in situ consolidated nanostructured Al and Al–Cr alloys produced via high-energy ball milling, Corrosion Sci. 98 (2015) 643–650, https://doi.org/10.1016/j.corsci.2015.06.011.

[40] P. Liu, Z. Wang, Y. Xiao, M.F. Horstemeyer, X. Cui, L. Chen, Insight into the mechanisms of columnar to equiaxed grain transition during metallic additive manufacturing, Addit. Manuf. 26 (2019) 22–29, https://doi.org/10.1016/j.addma.2018.12.019.